Combined FIB/SEM tomography and TEM analysis to characterize high aspect ratio Mg-silicate particles inside silica-based optical fibres

Martiane Cabié, Thomas Neisius, Wilfried Blanc

Combined FIB/SEM tomography and TEM analysis to characterize high aspect ratio Mg-silicate particles inside silica-based optical fibres

Martiane Cabié [a,*], Thomas Neisius [a], Wilfried Blanc [b]

[a] Aix Marseille Univ, CNRS, Centrale Marseille, FSCM, CP2M, 13397 Marseille, France
[b] Université Côte d'Azur, Institut de Physique de Nice (INPHYNI), CNRS UMR7010, Parc Valrose, 06108 Nice, France

ARTICLE INFO

Keywords:
FIB/SEM tomography
Transmission electron microscopy
Optical fibre
Phase separated particles
Elongation

ABSTRACT

The evolution of particles, during the fabrication step of particle-containing glass fibres, was investigated. The aim of this study was to characterize quantitatively the composition, size and shape distribution of Mg-silicate particles within the initial silica-based preform and the final fibre, these information being crucial to better understand the mechanisms involved during the drawing step. A combined experimental approach using Scanning electron microscopy, Transmission electron microscopy and FIB/SEM tomography was implemented. The particle composition was found to stay unchanged during the drawing step. On the other hand, strong modifications of their shape within the fibre is observed and discussed.

1. Introduction

In 1966, C.K. Kao and G.A. Hockam, published an article which has initiated the era of modern telecommunications based on optical fibres [1]. Since then, the paradigm was to increase the transparency of the fibre, and to develop fabrication processes for improved homogeneity of the glass. In the last twenty years, a reverse trend has been initiated by preparing heterogeneous glass, typically by adding nanoparticles in the fibre core [2]. Most of the optical fibres are based on silica glass which offers many advantages (mechanical, broad optical transparency window, low production cost, immunity to electromagnetic perturbation, biocompatibility, etc.). However, this type of glass suffers from drawbacks for luminescent ions such as rare-earth or metals ions (high phonon energy, low solubility, amorphous structure, etc.). Encapsulation of luminescent ions within nanoparticles of composition different from pure silica would allow to overcome those drawbacks and to tune their luminescent properties. Another field of interest for optical fibre containing nanoparticles is the recent development of distributed fibre sensors for temperature [3], 3D-shape sensing [4] or biomolecules detection [5].

While the drawing process is a homothetic transformation from the preform to the fibre (same core/cladding ratio), the behavior of nanoparticles is more complex during this step. Particles can elongate and even break-up into smaller particles due to Rayleigh-Plateau instability [6]. This phenomenon depends on a number of parameters including the size of the initial nanoparticles in the preform, the viscosity of the matrix and the nanoparticles and the surface tension of the silica-nanoparticle interface. Efficient tuning of light propagation in the fibre depends strongly on the ability to control the characteristics of the particles such as shape, chemical composition, size distribution and structure.

The characterization of nanoparticles doped optical fibres is a challenging task since the nanoparticles are confined in the core of the fibre with a relatively low density. A multitude of different methods are applied to get the most complete information. In order to determine the chemical composition of the nanoparticles and of the host material very often electron probe microanalysis [7], nanoSIMS [8] or atom probe tomography [9] are applied. Structural and/or morphological information is usually obtained by Scanning Electron Microscopy [10], X-ray Difffraction [11], Raman Spectroscopy [12] and Transmission Electron Microscopy [13]. Some of these methods have a probing volume bigger than the size of certain nanoparticles and are giving an averaged information, others have the necessary spatial resolution but are showing only a subset of the relevant structures. This is the case for nanoparticle doped silica fibres produced by using the drawing step, the structural information is spread over several orders of magnitude. The drawing step can lead to a combination of very small particles with a size below 100 nm and very elongated particles with a length of several microns while the diameter is ~100 nm.

In this work, we used several techniques based on electron microscopy to characterize the shape, composition, crystallinity of Mg-silicate

particles localized inside the core of silica-based preforms and fibres. Electron Micro Diffraction technique and STEM/EDX analyses were used to determine the particle structure and composition. After validating the spherical size of the nanoparticle inside the preform, the size distribution was extracted from SEM images using the Schwarz-Saltykov method to convert 2D to 3D size distribution. FIB/SEM tomography was performed in order to characterize the more complex shape of the particles inside the drawn fibre from the nanometre to the micrometre range. Special attention was given to the degradation of the glassy sample by the electron beam.

2. Experimental

2.1. Sample preparation

The fibre is obtained by drawing a rod of a 10 mm diameter, called the preform. This preform was fabricated using a conventional MCVD (Modified Chemical Vapor Deposition) process [14]. A GeO_2-doped silica porous core layer also containing phosphorus, was immersed in the doping solution for 3 h30. This solution was composed of a mixture of chloride salts $MgCl_2$ (1.5 mol/L) and $ErCl_3$ (0.01 mol/L), dissolved in ethanol. After the doping step, the porous layer has been sintered applying a temperature ramp up to 1800 °C. Then the tube collapsed into the final preform at a temperature above 2200 °C. The drawing of the fibre took place at a temperature around 2000 °C.

2.2. Transmission electron microscopy

Thin foils for TEM investigations were cut by FIB with a FEI dual beam Helios 600 Nanolab. These FIB lamellae were observed by TEM on a FEI Tecnaï G2 microscope equipped with a LaB_6 electron source operating at 200 kV. The composition was determined by STEM/EDX using an Energy Dispersive X-ray Detector (Oxford XMax 80). For quantitative chemical analysis we used the standardless Cliff-Lorimer method [15] as implemented in the Aztec software package from Oxford. Absorption was neglected.

Particular attention was paid to the choice of the acquisition conditions in order to limit beam damage of the samples. Indeed insulating materials are highly susceptible to electron-beam-induced damage mainly caused by the phenomena of radiolysis and electrostatic charging [16]. For this reason, the STEM/EDX analysis was operated in mapping mode, with a low electron current density and a short dwell-time of 5 µs. The probe was scanned several times over a square area of a few hundred nanometres square, including the particle and the surrounding glass matrix, for a total duration of 15 to 30 min. The composition of both the particle and the surrounding matrix was then extracted from the mapping by drawing two regions of interest (ROI) and accumulating the spectra acquired on all pixels included in the ROI.

The crystallinity of magnesium silicate particles was checked with the microdiffraction technique.

2.3. FIB/SEM 3D tomography

The tomography FIB/SEM analysis was performed on a FEI dual beam Helios 450 s microscope. The Auto Slice&View G3 software developed by FEI was used for automatic image acquisition and ion milling, and for autofocus and drift correction as well. The region of interest was prepared following the standard U-shape geometry. The experimental parameters were optimized to meet the constraints imposed by the system under study. They are listed in Table 1.

In order to acquire a larger area in the XY section plane (Fig. 1), without loss of spatial resolution, the tiling mode of the automatic acquisition software was used. This tiling was composed of two images of 13.5 by 9 µm with an overlap of 20%. These images will be referred as left and right image in the rest of the text.

As single glass fibres are non-conductive samples, SEM imaging at low accelerating voltage is recommended to reduce or avoid any charging effect. For the same reason imaging with backscattered electrons was preferred. Fig. 2 shows Monte Carlo simulations performed for two accelerating voltages (3 kV and 2 kV) in SiO_2 using the Casino software [17]. The corresponding escape depths of backscattered electrons are of the order of 25 and 10 nm, respectively. Due to a better contrast between the particles and the matrix, an accelerating voltage of 3 kV was chosen.

Following these conditions, the acquisition time required for one set of tiled images is around 10 min. 89 slices were acquired for a total time of 15 h.

The standard processing steps like background correction, noise reduction, alignment, stitching, segmentation and quantification were done by the freely available ImageJ software packet. For 3D visualization the commercial Amira software was used.

As seen in Fig. 3a, a non-uniform contrast gradient is visible from the top to the bottom of the viewing area. This effect is due to a shadowing of the signal coming from the bottom of the section according to the position of the in-lens detector. This effect was corrected by subtracting from the original image a low frequency background obtained by filtering with a Gaussian filter (Fig. 3b).

The image brightness and contrast can differ slightly from one image to another inside the stack. The *Stack Contrast Adjustment* correction available as plugin for ImageJ was applied [18]. The first image of the stack was chosen as reference.

In order to reduce the noise in the images, a sigma filter [19] followed by a non-local mean denoising filter [20–22] were successively applied. This noise reduction is clearly visible in Fig. 3c. In addition, line profiles drawn across an elongated particle confirm that the noise is strongly reduced while particle edges are preserved (Fig. 3d). However, this filtering lead to a small reduction of the contrast between the particle and the glass matrix.

The sequential layers of the left part of the tiling were aligned using

Table 1
Acquisition conditions for FIB/SEM tomography.

FIB		SEM	
Voltage (kV)	30	Voltage (kV)	3
Current (pA)	90	Current (nA)	0.8
z spacing (nm)	10	x pixel size (nm)	9
		Beam dwell time (µs)	100

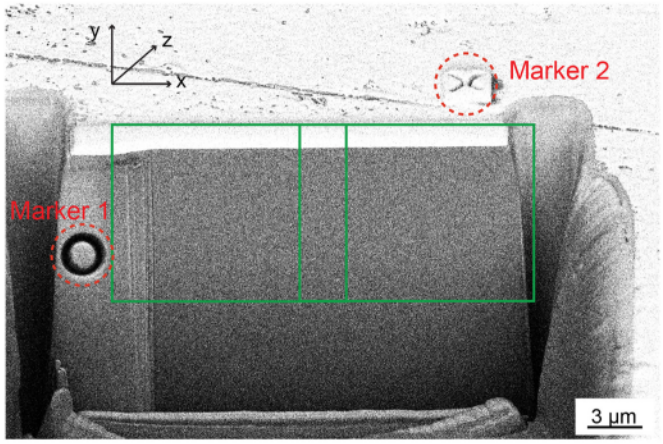

Fig. 1. U-shape geometry for 3D FIB/SEM tomography. XY is the imaging plane and Z direction is the slicing direction. Green boxes represent the left and right images of the tiling. Marker 1 was specifically prepared in order to facilitate the alignment procedure of the SEM images. Marker 2 enables aligning the ion beam for the milling. (For interpretation of the references to colour in this figure legend, the reader is referred to the web version of this article.)

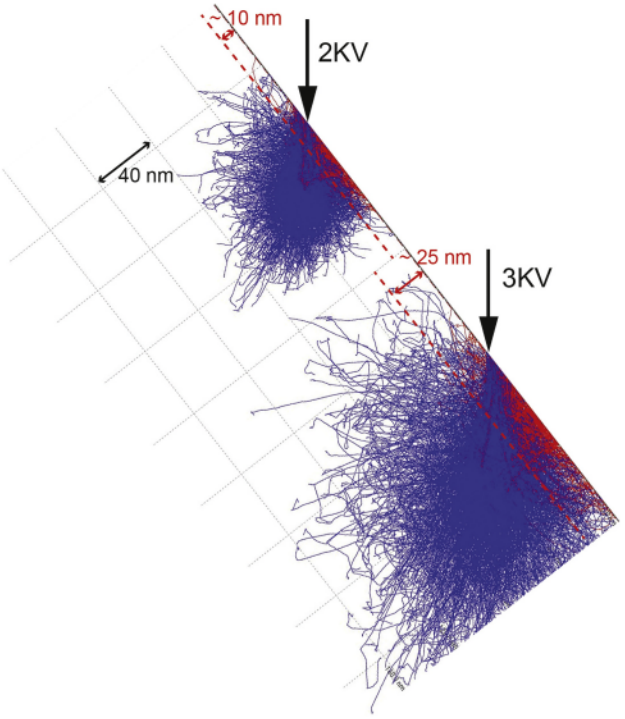

Fig. 2. Electron trajectories in SiO_2 calculated by Monte Carlo simulations. The blue and red trajectories represent the track of penetrating electrons and the BSE, respectively. The escape depth of BSE (indicated by the length between red arrows) are reduced from 25 nm to 10 nm when the accelerating voltage is reduced from 3 to 2 kV. (For interpretation of the references to colour in this figure legend, the reader is referred to the web version of this article.)

the ImageJ plugin *Multistackreg* [23]. The alignment with a translation-type transformation was first applied to a specific ROI of the stack. After having obtained a satisfying result, the same transformation was applied to the whole stack. Indeed, the elongated shapes of some particles are not well suited to the cross-correlation process required for the correction. As a consequence, this can lead to an erroneous result. ROI's containing no or only few elongated particles were favoured.

The next processing step is the stitching of the left and right parts of the tiling. The same processing steps applied to the left stack were applied to the right one, except alignment. After normalising the mean intensity of both stacks, the images were stitched semi-automatically one by one with the help of the MosaicJ plugin [24].

Finally, segmentation was achieved using the *Autothreshold* plugin proposed by imageJ which consists of 16 histogram-based automatic methods. Among all these algorithms, 5 methods (Default, Huang, Max Entropy, RenyiEntropy and Yen) gave very similar results. The Huang algorithm was arbitrarily chosen (Fig. 4).

The resolution in the X-Y-plane of the final stitched stack, depending on the SEM imaging resolution, is 9 nm. The Z resolution corresponding to the chosen distance between two slices is 10 nm. For visualization, the Amira software uses cubic voxels. Consequently, a linear interpolation between adjacent slices has to be applied so that the Z step becomes the same as the X and Y pixel size. This correction was performed with the *Adjust Size* function of imageJ. The diameter of spherical particles was determined using the *3D Object Counter* plugin [25].

3. Results and discussion

3.1. Preform

Fig. 5 is observed at the central area of the preform imaged at 3 kV by SEM with backscattered electrons. The particles appear in white contrast

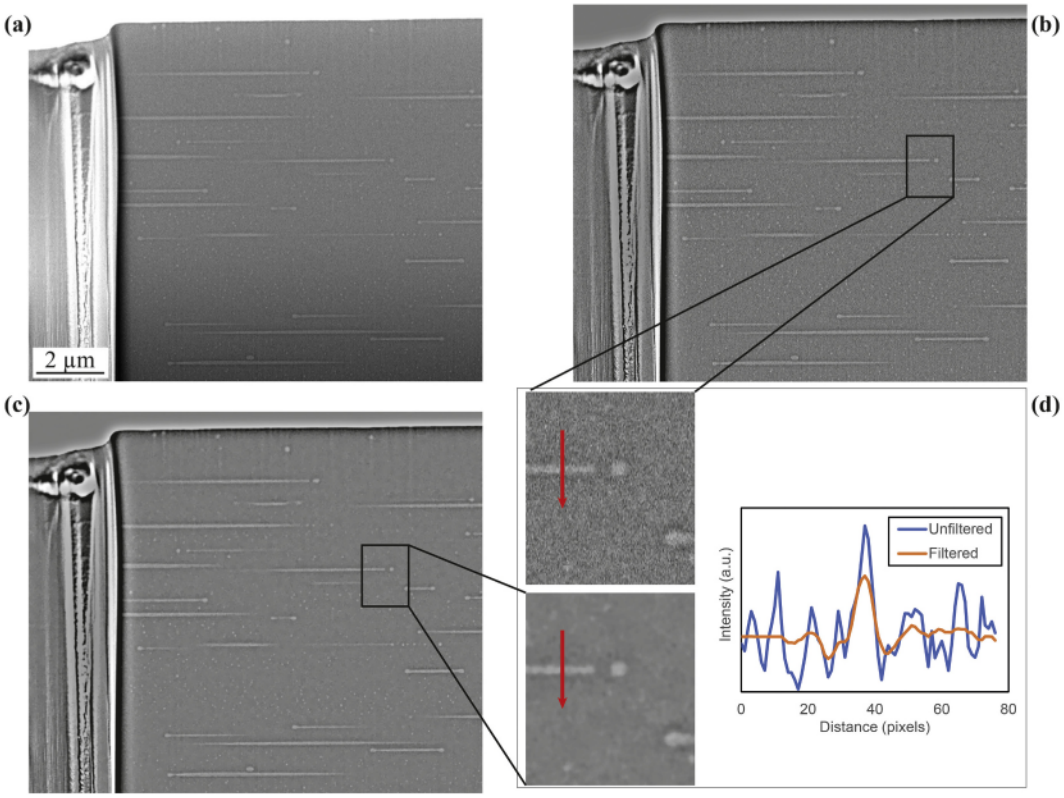

Fig. 3. (a) Original SEM image. (b) Background corrected image. (c) Filtered image after noise reduction. (d) Intensity line profile drawn along the red arrows crossing the elongated particle shown in the magnified inserts of images (b) and (c). (For interpretation of the references to colour in this figure legend, the reader is referred to the web version of this article.)

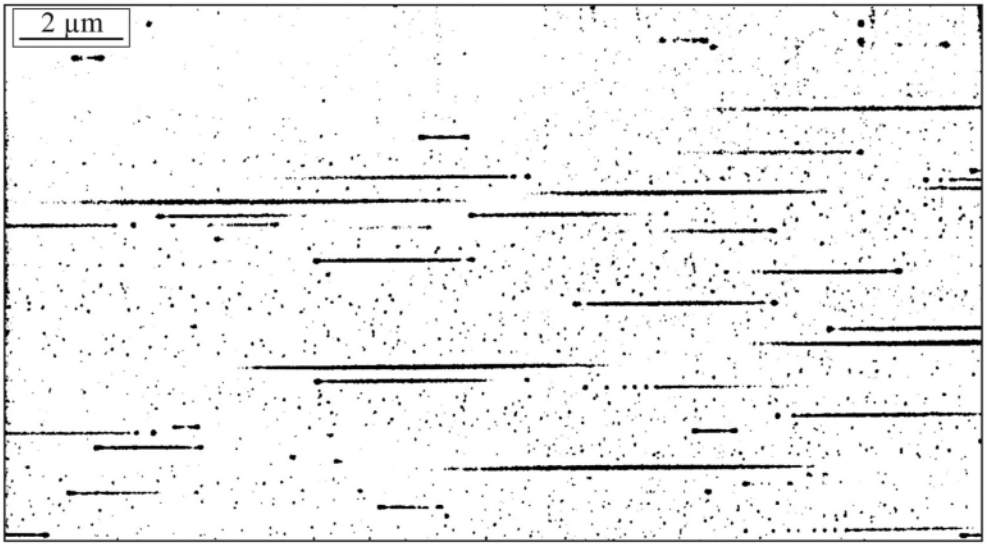

Fig. 4. Automatic threshold image.

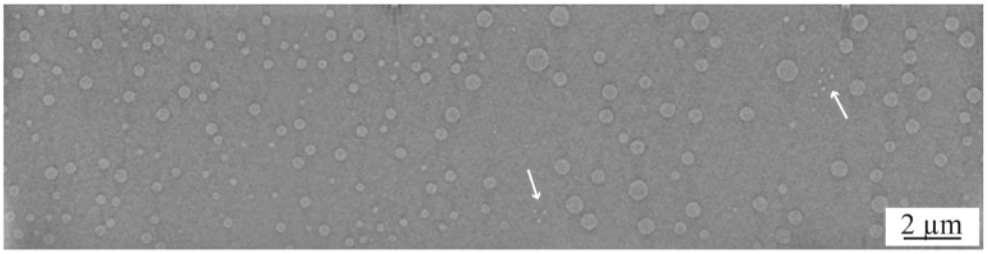

Fig. 5. Typical BSE image of the central part of the preform. Arrows indicate particle sections representative of the smallest class.

on a dark background corresponding to the surrounding glass matrix. The particles are polydispersed and ranged in 3 main size classes: largest and medium particle sections are located on the right and left part of the image, respectively. The smallest particles sections are identified by arrows.

As the section shape of these particles is circular, independently of the observed section plane (either perpendicular or parallel to the fibre axis), we can conclude that these particles are spherical. The Schwarz-Saltykov [26,27] method is applied to estimate the 3D size distribution using the 2D section-size distribution measured on SEM images. This technique is a classical stereology procedure based on the following relation:

$$Nv(j) = \frac{1}{\Delta}\sum_{i=1}^{k} \propto_{ij} Na(i) \quad (1)$$

Where Na(i) is the number of particle sections per unit area in each class i of the 2D distribution, Nv(j) is the number of particles per unit volume in each class j of the 3D distribution and α_{ij} are coefficients derived from geometrical and probabilistic considerations. The values of i and j are up to a maximum value of k defined as

$$\Delta = \frac{D}{k} \quad (2)$$

where D refers to the maximum diameter of the measured sections and Δ is the width of the class. The calculation of the α_{ij} coefficients is described in detail in Reference [28].

For the 2D-3D transition in our work, the maximal 2D diameter is equal to 714 nm. The number k of classes was fixed to 15, given a Δ of 50 nm. A total of 551 particles were analysed on a section area of 843 μm^2. Negative values were observed in the lower histogram. They are not shown in the graph. They are probably due to the small particle numbers in these lowest classes. This so-called "oversight-effect" is a well-known artefact of the Schwarz-Saltykov method as described in [28]. In the 2D particle size distribution, sections in a given class of diameter are originating from: i) particles from the same diameter which are intersected at their equatorial plane or ii) particles having greater diameters intersected above or under their equatorial plane. When applying the Schwartz-Saltykov method to estimate the 3D size distribution, the number of particles in a class j is calculated by subtracting from the number of particles of the same diameter, the number of particles in bigger classes multiplied by the probability that they have generated a section in this class j. This subtraction can lead to negative values in the case that only a few sections are counted for these classes in the 2D distribution.

In our case, these few sections in the lower part of the 2D histogram can be explained by either the presence of only a small number of particles are in these classes or by the weak contrast of these sections in the 2D SEM compared to the bigger ones, which makes the extraction from the background more difficult.

Fig. 6b represents the size distribution of particles inside the preform. These spherical particles are highly dispersed with diameters ranging from 100 to 750 nm.

The volume fraction of particles deduced from these results is equal to 5.8 ± 1.0%.

Fig. 7 is a representative EDX spectrum measured on ~20 particles located at the center of the preform. The main peaks are attributed to O, Mg, Si and P elements. A fourth peak, corresponding to Er L-line, was sometimes visible. However due to its low count rate, this element was not quantified. The measured composition varies slightly from one particle to another, the differences are within the error bar. The mean

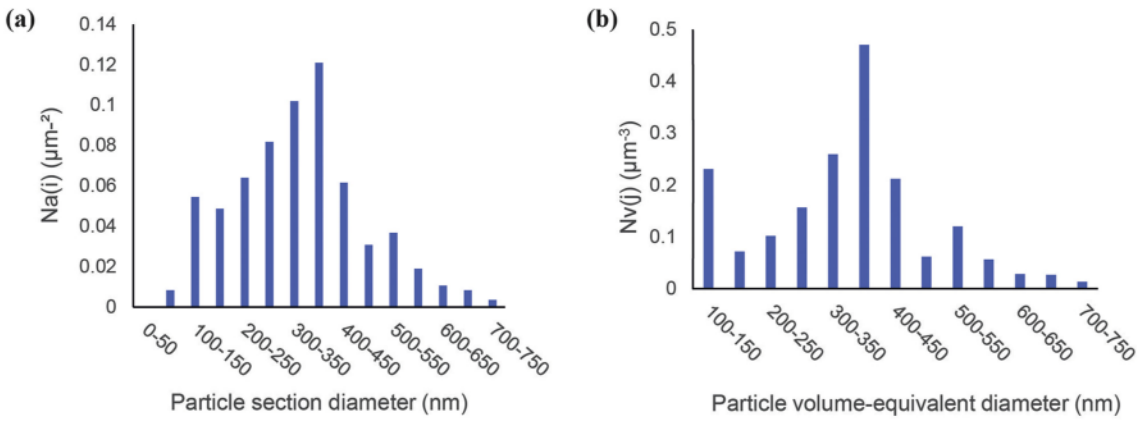

Fig. 6. (a) 2D size distribution. (b) 3D size distribution calculated from the 2D size distribution using the Schwarz-Saltykov conversion method.

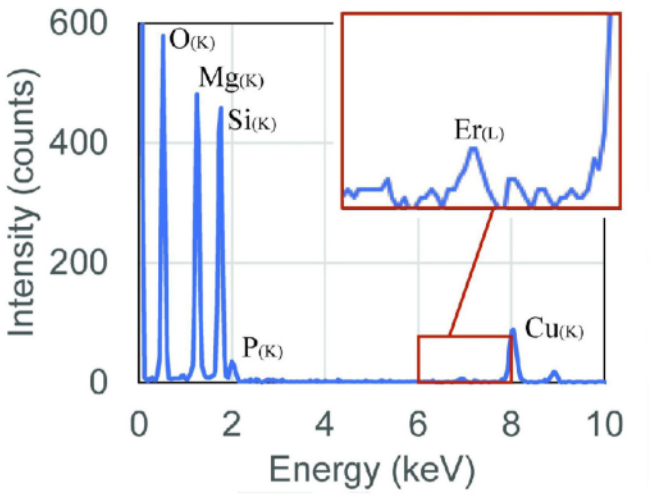

Fig. 7. Typical EDX spectrum measured by STEM/EDX on the particles in the preform.

content of O, Mg, Si and P are equal to 58.1, 21.2, 19.3 and 1.4 atomic percent (at.%) respectively. This composition is coherent with the enstatic phase $Mg(Si + P)O_3$, with a $Mg/(Si + P)$ concentration ratio close to 1. The composition of the glass matrix deduced from the O(K) and Si(K) fluorescence peaks is equal to 66 and 34 at.% respectively, in very good agreement with the silica glass stoichiometry. This indicates that most of Mg and P atoms are located inside the particles. Surprisingly, no Ge peak is visible in the spectra. This result can be explained by the high temperatures used during the fabrication of the preform, which may cause the evaporation of germanium.

For these measurements, the transmission geometry was chosen to suppress in the most efficient way the contribution from the matrix to the x-ray fluorescence signal. Indeed, one well-known limitation of SEM-EDX is a large electron interaction volume. As illustrated in Fig. 2, even at low accelerating voltages the electrons penetrate deeper than 150 nm. This depth is on the order of µm for the energies commonly used for SEM-EDX analyses. The interaction volume is considerably smaller in STEM where the penetration depth is reduced to the thickness of the sample. In our case the samples were prepared by FIB and their thickness was approximately 150 nm. Only particles crossing entirely the thickness of the sample were analysed. This requirement was checked, before STEM/EDX analysis, by taking SEM images of the two faces of the FIB lamella at low voltage. Particles visible on both faces were selected.

Micro-diffraction patterns taken from about ten particles indicate these particles are amorphous in the preform (Fig. 8).

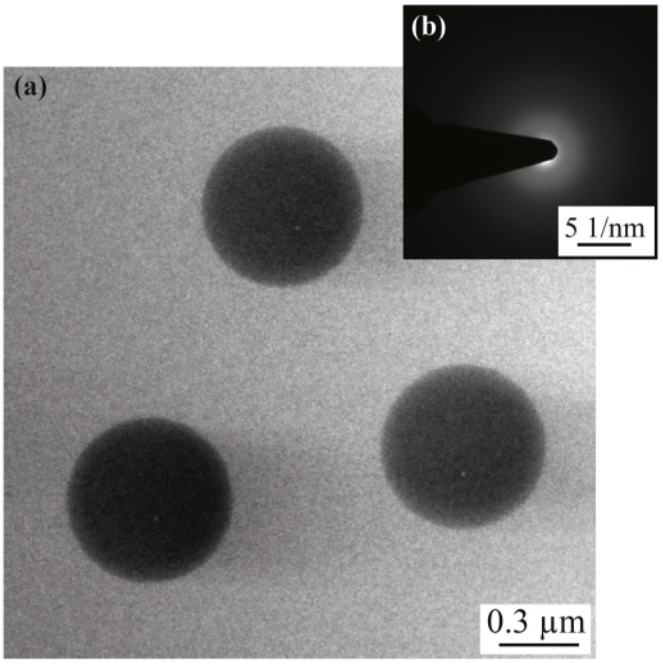

Fig. 8. (a) Bright field TEM image of a preform sample. (b) Diffraction pattern of the particle on top of image (a).

3.2. *Fibre*

Particles are no longer spherical as illustrated in Fig. 3 showing SEM image of a transversal section of the central part of the fibre. They exhibit different shapes. This will be studied in more details in the following section.

The chemical composition of the particles was measured by STEM-EDX on a lamella cut by FIB perpendicularly to the axis of the fibre. This geometry ensures that elongated particles cross entirely the thickness of the lamella, a requirement necessary to avoid any contribution from the glass matrix, as explained in part 3–1. The shape of the intensity profile (Fig. 9) drawn along the particles diameter enables to distinguish between elongated particles cut by the FIB preparation (hat profile) and spherical particles embedded inside the glass matrix (bell-shaped profile). For the reasons stated above, only the elongated particles were analysed by STEM-EDX.

The EDX spectrum is similar to the one measured in the preform. The particle composition is identical to the composition of the enstatic phase already measured in the preform. The partition of these elements in

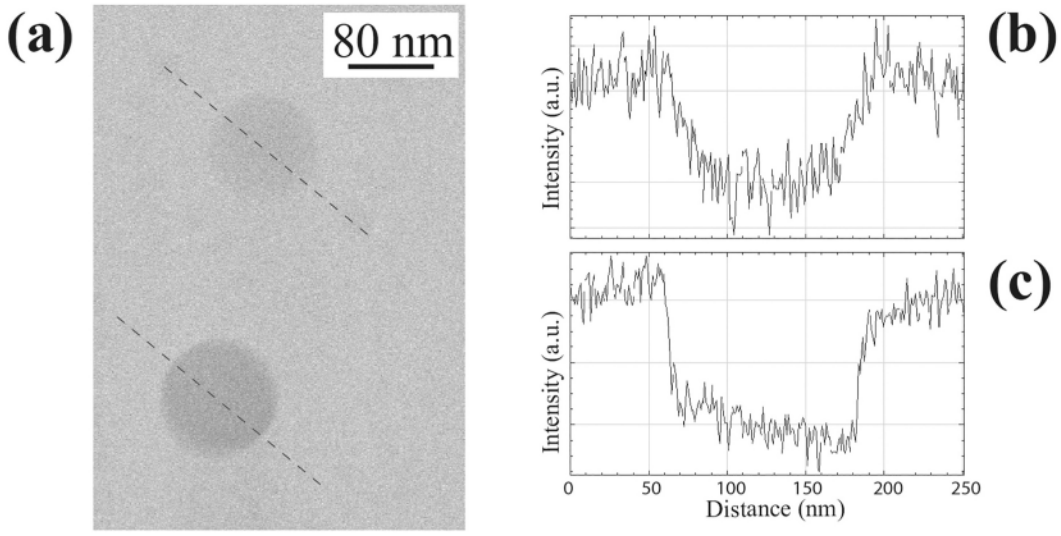

Fig. 9. (a) Cross-section bright field STEM image observed on a FIB lamella taken from the fibre core. Intensity line profiles drawn following the dashed lines in image (a) across a spherical particle (particle on the top of (a)) (b) and an elongated particle (on the bottom of the image (a)) truncated by both faces of the FIB lamella (c).

nanoparticles is in accordance with Atom Probe Tomography analyses of small nanoparticles [9]. However, we noticed that, even if the Si/P concentration ratio remained constant, the P concentration varied from 1.1 at.% to 10.7 at.% depending on the particle analysed. This dispersion was correlated to the radial position of the particle inside the fibre core. As illustrated in Fig. 10a, particles close to the core centre exhibit a P concentration below 2 at. %, while particles located further have a higher P concentration ($\geq$ 2 at.%).

In order to check if this variation of the phosphorus concentration as a function of the radial position is due to an initial concentration gradient inside the preform or to a modification of the particle composition during the drawing step, different FIB lamellas were cut in the preform, at different radial positions (0R, 0.45R and 0.9R). For each lamella, a tens of particles were analysed by EDX in order to determine an average concentration of phosphorus for a given radial position. The results reported in Fig. 10b show that the same phosphorus gradient is observed in the preform too. This result demonstrates that the composition of the largest particles remains unchanged during the drawing step.

TEM microdiffraction analysis (not shown) indicates that these particles are amorphous.

The morphology of these particles was studied by FIB/SEM tomography. A 3D rendering of the particles is presented in Fig. 11. The total reconstructed volume is equal to 19 µm by 10.4 µm by 0.7 µm. For reasons of clarity, only particles larger than 70 nm are shown. Particles smaller than 70 nm have spherical shape, within the limit of the spatial resolution. In Fig. 11, we can distinguish elongated particles with a dumbbell shape. Some of them present, on both sides, chains of monodispersed nanoparticles homogeneously spaced. Other particles, less numerous, have undergone coalescence or correspond to isolated spherical particles The elongation factor of dumbbell shaped particles is in between 4 and 69 with an average value of 26. Elongated particles that have undergone fragmentation show a higher aspect ratio with an elongation factor in between 49 and 111 and an average value of 78. This last value is probably underestimated do to the limited reconstructed volume. The particle size distribution is represented in Fig. 12. In order to compare with this distribution with the distribution of particles in the preform, the particle size is represented by the Equivalent Spherical Diameter (ESD).

The ESD of the elongated particles is calculated from the volume of

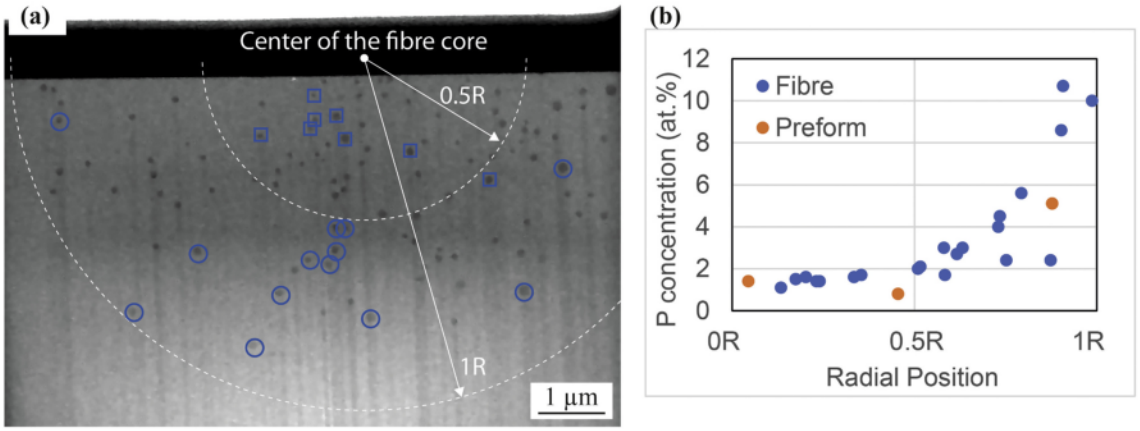

Fig. 10. (a) Low magnification bright field STEM image of the FIB lamella taken from the fibre core. The dark layer on top of the lamella is a protective platinum layer. Particles framed by a circle show the lowest phosphorus content and are located closer to the centre of the core. Particles framed by a square contain more than 2 atomic percent of phosphorus. They are located beyond 0.5R from the centre, where R is the core radius. (b) Variation of the phosphorus content as a function of the radial position of particles inside the fibre and the preform.

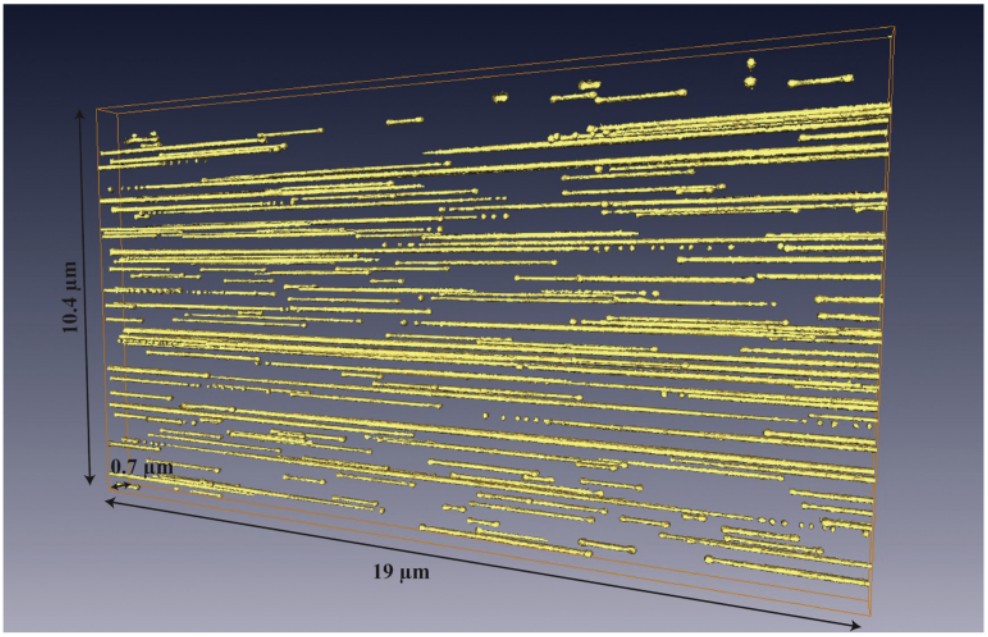

Fig. 11. 3D rendering of particles. Smaller spherical particles, randomly distributed, are not represented.

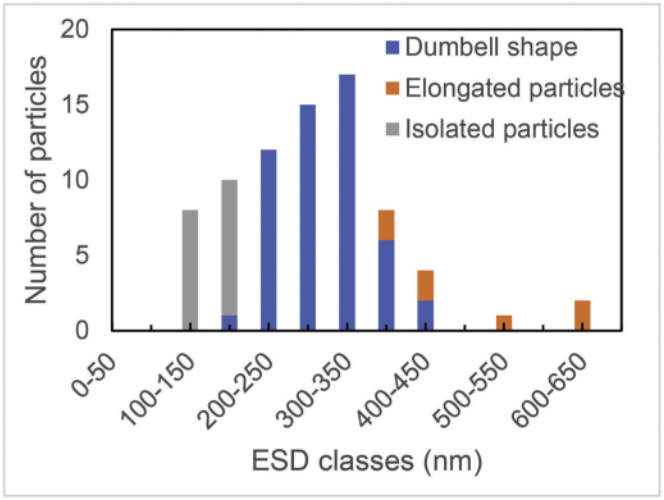

Fig. 12. 3D size distribution of particles inside the fibre. A different colour is used for each type of morphology. Particles with an ESD smaller than 100 nm are not represented.

the central elongated part plus the volume of the chains of monodispersed particles on either side. The right part of this distribution for ESD classes greater than 350 nm is distorted by the lack of elongated particles cut by the faces of the limited reconstructed volume. However, qualitatively, this shows that the elongated particles have their origin in particles in the preform in the range from 350 to more than 650 nm. The dumbbell shaped particles have been created from particles in the range from 150 to 450 nm. In addition, isolated particles, with an ESD in between 100 and 200 nm are probably too small to undergo an elongation.

An elongation similar to the one observed in this article has been reported by the group of Blanc [6]. The authors state that these shape changes are governed by rheological mechanisms, triggered by Rayleigh-Plateau capillary instabilities which causes the elongation and the fragmentation of particles. Indeed, during the drawing step, the silica-based preform is heated up to a temperature of approximately 2000 °C, well above its softening temperature. As a consequence, glass becomes viscous and flows. The viscous forces applied on the particles will tend to elongate their shape but their surface tension will favour a spherical shape. For more details, the interested reader should refer to the study of Vermillac [6]; and references therein. This effect could be a promising way to tune the particle size inside the fibre as proposed in reference [29].

In the reconstructed volume, the total volume occupied by the particles is equal to 4.8 μm^3, giving a volume fraction of the particles equal to 3.6 ± 0,7%. This volume fraction is smaller than the one calculated for the preform (F_V(preform) = 5.8 ± 1.0%). This can be explained by the presence of smaller spherical particles, randomly distributed inside the fibre core (see Fig. 3). For reasons of clarity, these particles are not shown either in the 3D rendering or in the size distribution. Their volume fraction determined on a part of the whole reconstructed volume is equal to 1.0 ± 0.2%. The total volume fraction occupied by the particles is then equal to 4.6 ± 0.9%, which is in good agreement with the volume fraction in the preform. The origin of the nanoparticles is still unclear. Some hypotheses can be proposed. As the initial particles are heated to a temperature of 2000 °C for 2 to 3 min during the drawing step, it is possible that some of them melt and reform smaller particles. Another explanation could be a complete dissolution of some particles followed by the formation of new particles, during the cooling. A further growing of these particles could be supressed by the quenching.

Compared to previous studies [6,29], the comparative analysis of the preform and of the fibre carried out in this article makes it possible to improve our knowledge with regard to the effect of drawing on nanoparticles. Thanks to the large volume probed in the fibres, we could show the link between the initial size of the particles in the preform and the final shape of the particles in the fibre. The volume fraction and the composition of the larger particles being retained during drawing, the change in shape can be explained mainly by mechanical effects under these drawing conditions. These results show that drawing can be used to effectively control the characteristics of the particles in the fibre.

4. Conclusion

Several characterization methods including FIB/SEM tomography and TEM were combined to determine the composition, shape, crystallinity and size distribution of Mg-silicate particles in silica-based optical fibres and in the initial preform. Particles are found to be amorphous with the composition of the enstatic phase both in the preform and in the

fibre. The P content is equal to 1.4 at.% for particles in the preform and varies from 1.1 to 10.7 at.% in the fibre. These results demonstrate that for particles larger than 100 nm, their composition remains unchanged during the drawing step. The particle shape in the preform and the fibre are completely different. In the preform particles are initially spherical and polydispersed with diameters ranging from 100 to 750 nm. More complex shapes governed by rheological mechanisms and nanoparticles randomly dispersed were observed in the fibre. FIB/SEM tomography is an unavoidable tool for the 3D characterization of embedded particles with such morphologies, including both spherical particles with dimensions as small as a few tens of nanometres and elongated particles with volume aspect ratio as high as 200. Even if other methods like X-ray nanotomography could offer a better statistic, FIB/SEM tomography offers the advantages of a good spatial resolution and a high particles/matrix sensitivity in the case of close chemical composition.

Funding

This work was supported by the Nanoslim ANR-17-CE08-0002-05 project granted by The French National Research Agency.

Data availability statement

The raw data required to reproduce these findings cannot be shared at this time as the data also forms part of an ongoing study.

Declaration of Competing Interest

The authors declare that they have no known competing financial interests or personal relationships that could have appeared to influence the work reported in this paper.

Acknowledgments

The authors thank Michèle Ude and Stanislaw Trzesien (INPHYNI, Nice,France) for the preparation of the preform and the fibre.

References

[1] K.C. Kao, Dielectric-Fibre Surface Waveguides for Optical Frequencies 113, 1966, p. 8.

[2] A. Veber, Z. Lu, M. Vermillac, F. Pigeonneau, W. Blanc, L. Petit, Nano-structured optical fibers made of glass-ceramics, and phase separated and metallic particle-containing glasses, Fibers. 7 (2019) 105, https://doi.org/10.3390/fib7120105.

[3] Z. Ashikbayeva, A. Aitkulov, M. Jelbuldina, A. Issatayeva, A. Beisenova, C. Molardi, P. Saccomandi, W. Blanc, V.J. Inglezakis, D. Tosi, Distributed 2D temperature sensing during nanoparticles assisted laser ablation by means of high-scattering fiber sensors, Sci. Rep. 10 (2020) 12593, https://doi.org/10.1038/s41598-020-69384-2.

[4] A. Beisenova, A. Issatayeva, I. Iordachita, W. Blanc, C. Molardi, D. Tosi, Distributed fiber optics 3D shape sensing by means of high scattering NP-doped fibers simultaneous spatial multiplexing, Opt. Express 27 (2019) 22074, https://doi.org/10.1364/OE.27.022074.

[5] M. Sypabekova, A. Aitkulov, W. Blanc, D. Tosi, Reflector-less nanoparticles doped optical fiber biosensor for the detection of proteins: case thrombin, Biosens. Bioelectron. 165 (2020) 112365, https://doi.org/10.1016/j.bios.2020.112365.

[6] M. Vermillac, J.-F. Lupi, F. Peters, M. Cabié, P. Vennéguès, C. Kucera, T. Neisius, J. Ballato, W. Blanc, Fiber-draw-induced elongation and break-up of particles inside the core of a silica-based optical fiber, J. Am. Ceram. Soc. 100 (2017) 1814–1819, https://doi.org/10.1111/jace.14774.

[7] S. Kang, Z. Fang, X. Huang, Z. Chen, D. Yang, X. Xiao, J. Qiu, G. Dong, Precisely controllable fabrication of Er3+−doped glass ceramic fibers: novel mid-infrared fiber laser materials, J. Mater. Chem. C 5 (2017) 4549–4556, https://doi.org/10.1039/C7TC00988G.

[8] W. Blanc, C. Guillermier, B. Dussardier, Composition of nanoparticles in optical fibers by secondary ion mass spectrometry, Opt. Mater. Express. 2 (2012) 1504, https://doi.org/10.1364/OME.2.001504.

[9] W. Blanc, I. Martin, H. Francois-Saint-Cyr, X. Bidault, S. Chaussedent, C. Hombourger, S. Lacomme, P. Le Coustumer, D.R. Neuville, D.J. Larson, T. J. Prosa, C. Guillermier, Compositional changes at the early stages of nanoparticles growth in glasses, J. Phys. Chem. C 123 (2019) 29008–29014, https://doi.org/10.1021/acs.jpcc.9b08577.

[10] M. Tuggle, T.W. Hawkins, C. Kucera, N. Huygen, A. Brasovs, K. Kornev, J. Ballato, Phase separation and transformation of binary immiscible systems in molten core-derived optical fibers, MRS Commun. 10 (2020) 298–304, https://doi.org/10.1557/mrc.2020.20.

[11] G. Gorni, R. Balda, J. Fernández, I. Iparraguirre, J.J. Velázquez, Y. Castro, L. Pascual, G. Chen, M. Sundararajan, M.J. Pascual, A. Durán, Oxyfluoride glass–ceramic fibers doped with Nd3+: structural and optical characterization, CrystEngComm. 19 (2017) 6620–6629, https://doi.org/10.1039/C7CE01380A.

[12] D.D. Genova, R.A. Brooker, H.M. Mader, J.W.E. Drewitt, A. Longo, J. Deubener, D. R. Neuville, S. Fanara, O. Shebanova, S. Anzellini, F. Arzilli, E.C. Bamber, L. Hennet, G.L. Spina, N. Miyajima, In situ observation of nanolite growth in volcanic melt: a driving force for explosive eruptions, Sci. Adv. 6 (2020), eabb0413, https://doi.org/10.1126/sciadv.abb0413.

[13] M.W. Sckerl, S. Guldberg-Kjaer, M. Rysholt Poulsen, P. Shi, J. Chevallier, Precipitate coarsening and self organization in erbium-doped silica, Phys. Rev. B 59 (1999) 13494–13497, https://doi.org/10.1103/PhysRevB.59.13494.

[14] J.B. MacChesney, P.B. O'Connor, H.M. Presby, A new technique for the preparation of low-loss and graded-index optical fibers, Proc. IEEE 62 (1974) 1280–1281, https://doi.org/10.1109/PROC.1974.9608.

[15] G. Cliff, G.W. Lorimer, The quantitative analysis of thin specimens, J. Microsc. 103 (1975) 203–207, https://doi.org/10.1111/j.1365-2818.1975.tb03895.x.

[16] N. Jiang, Electron beam damage in oxides: a review, Rep. Prog. Phys. 79 (2015), 016501, https://doi.org/10.1088/0034-4885/79/1/016501.

[17] D. Drouin, A.R. Couture, D. Joly, X. Tastet, V. Aimez, R. Gauvin, CASINO V2.42—A fast and easy-to-use modeling tool for scanning electron microscopy and microanalysis users, Scanning. 29 (2007) 92–101, https://doi.org/10.1002/sca.20000.

[18] M. Čapek, J. Janáček, L. Kubínová, Methods for compensation of the light attenuation with depth of images captured by a confocal microscope, Microsc. Res. Tech. 69 (2006) 624–635, https://doi.org/10.1002/jemt.20330.

[19] J.-S. Lee, Digital image smoothing and the sigma filter, Comp. Vision Graphics Image Proc. 24 (1983) 255–269, https://doi.org/10.1016/0734-189X(83)90047-6.

[20] A. Buades, B. Coll, J.-M. Morel, Non-local means denoising, Image Proc. On Line. 1 (2011) 208–212, https://doi.org/10.5201/ipol.2011.bcm_nlm.

[21] J. Darbon, A. Cunha, T.F. Chan, S. Osher, G.J. Jensen, Fast nonlocal filtering applied to electron cryomicroscopy, in: 2008 5th IEEE International Symposium on Biomedical Imaging: From Nano to Macro, 2008, pp. 1331–1334, https://doi.org/10.1109/ISBI.2008.4541250.

[22] T. Wagner, P. Behnel, Non Local Means Denoise - Implementation (https://zenodo.org/record/47468#.X84EebPjKM8), visited on 23/11/2020, (2020).

[23] P. Thevenaz, U.E. Ruttimann, M. Unser, A pyramid approach to subpixel registration based on intensity, IEEE Trans. Image Process. 7 (1998) 27–41, https://doi.org/10.1109/83.650848.

[24] P. Thévenaz, M. Unser, User-friendly semiautomated assembly of accurate image mosaics in microscopy, Microsc. Res. Tech. 70 (2007) 135–146, https://doi.org/10.1002/jemt.20393.

[25] S. Bolte, F.P. Cordelières, A guided tour into subcellular colocalization analysis in light microscopy, J. Microsc. 224 (2006) 213–232, https://doi.org/10.1111/j.1365-2818.2006.01706.x.

[26] S.A. Saltykov, Stereometric Metallurgy, Armed Services Technical Information Agency, Arlington, Va, 1961.

[27] S.A. Saltykov, A stereologycal method for measuring the specific surface area of metallic powders, in: Stereology: Proceedings of the Second International Congress for STEREOLOGY, Chicago—April 8–13, 1967, Springer-Verlag, Berlin Heidelberg, 1967, pp. 63–64, https://doi.org/10.1007/978-3-642-88260-9.

[28] J. Takahashi, H. Suito, Evaluation of the accuracy of the three-dimensional size distribution estimated from the schwartz-saltykov method, Metall Mat. Trans. A. 34 (2003) 171–181, https://doi.org/10.1007/s11661-003-0218-6.

[29] M. Vermillac, H. Fneich, J. Turlier, M. Cabié, C. Kucera, D. Borschneck, F. Peters, P. Vennéguès, T. Neisius, S. Chaussedent, D.R. Neuville, A. Mehdi, J. Ballato, W. Blanc, On the morphologies of oxides particles in optical fibers: effect of the drawing tension and composition, Opt. Mater. 87 (2019) 74–79, https://doi.org/10.1016/j.optmat.2018.05.067.